Tuning the Mn and Fe valence states into new Ca0.7Mn2-xFexO4 (0 < x £ 0.60) solid solution during reversible redox processes

Stéphanie Lesturgez, Graziella Goglio, Mathieu Duttine, Alain Wattiaux, Etienne Durand, Julien Hernandez, Jérôme Majimel, Alain Demourgues

Stéphanie Lesturgez, Graziella Goglio, Mathieu Duttine, Alain Wattiaux, Etienne Durand, Julien Hernandez, Jérôme Majimel and Alain Demourgues*

Chem. Mater. **2016**, *xx*, xxxx

Tuning the Mn and Fe Valence States into New $Ca_{0.7}Mn_{2-x}Fe_xO_4$ ($0 < x \leq 0.60$) Solid Solution during Reversible Redox Processes.

The Fe^{3+} substitution for Mn^{4+}/Mn^{3+} into new $Ca_{0.7}Mn_{2-x}Fe_xO_4$ 1D tunnel network leads to the stabilization of an orthorhombic unit cell (SG : Pnma) with two various Mn site attributed mainly to $Mn^{4+}/Mn^{3+}/Fe^{3+}$ and Mn^{3+}/Fe^{3+} respectively. The higher the Fe content, the higher the Mn valence state and the lower the Mn^{3+} Jahn-Teller distortion. Redox cycling properties between these $Mn^{4+}/Mn^{3+}/Fe^{3+}$ oxides and Mn^{2+}/Fe^{2+} rocksalt solid solution with metal Fe^0 as second phase have been demonstrated by preserving two Fe sites with various distortion.

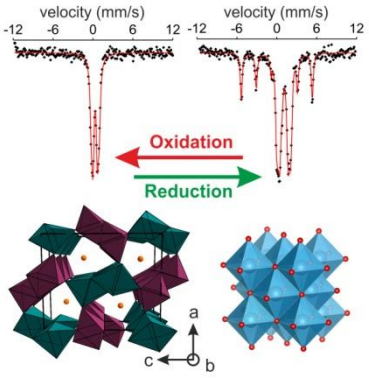

Tuning the Mn and Fe Valence States into New $Ca_{0.7}Mn_{2-x}Fe_xO_4$ ($0 < x \leq 0.60$) Solid Solution during Reversible Redox Processes

Stéphanie Lesturgez,[1,2] Graziella Goglio,[1] Mathieu Duttine,[1] Alain Wattiaux,[1] Etienne Durand,[1] Julien Hernandez,[2] Jérôme Majimel,[1] Alain Demourgues,[1,*]

[1]CNRS, Univ. Bordeaux, ICMCB, UPR 9048, F-33600 Pessac, France

[2]SOLVAY, Centre de Recherche et Innovation de Paris Aubervilliers, 52 Rue de la Haie Coq, 93306 Aubervilliers Cedex, France

ABSTRACT: New Mn^{4+}-rich $Ca_{0.7}Mn_{2-x}Fe_xO_4$ complex oxides ($0 < x \leq 0.6$) with Mn^{4+} amount varying from 33% to 43% have been prepared by aqueous self-combustion routes and characterized by powder X-Ray Diffraction (XRD) and Mössbauer spectroscopy. These oxides crystallize with a monoclinic symmetry ($CaMn_3O_6$-type, SG: P21/a) for low Fe content and with an orthorhombic symmetry ($CaFe_2O_4$-type, SG: Pnma) for $x > 0.14$, thus stabilizing the highest Ca defects content (30%) for this series. A regular decrease of the Jahn-Teller Mn^{3+} site distortion is observed versus Fe content. For low iron content ($x < 0.33$), Fe^{3+} ions are preferentially but not exclusively located at the Mn^{4+}-rich site which exhibits lower octahedral distortion whereas, for higher iron doping-rate ($x \geq 0.33$), Fe^{3+} ions are almost equally distributed in the two more or less distorted transition metal sites. The same distribution of Fe^{3+} in both of these atomic positions contributes to the stabilization within these phases of a high content of Mn^{4+} even at higher temperatures ($T > 1000°C$) whereas the un-substituted $Ca_{0.66}Mn_2O_4$ phase is only stable up to 850°C. Furthermore, these phases can be reduced at T=550°C under Ar/5% H_2 into a Mn^{2+} and Fe^{2+}/Fe^{3+} phase based on the rocksalt structure and then, re-oxidized at T=700°C under air to get pure phases with the same orthorhombic unit cell and a Fe^{3+} distribution in the two atomic positions similar to the initial phase. Despite the additional stabilization of metal iron Fe^0 during the reduction at T>550°C, a pure $Mn^{4+}/Mn^{3+}/Fe^{3+}$-based oxide with $CaFe_2O_4$-type structure has been recovered after oxidation at T>700°C under air. Mössbauer spectroscopy of the reduced phase has revealed the presence of Fe^{2+} ions at two distinct octahedral sites corresponding to Fe^{3+} within the oxidized phase. The reversibility of this redox system could be explained by the occurrence of two rutile double chains in the $CaFe_2O_4$-type network, which is closely related to the rocksalt structure with Ca^{2+} ions in the vicinity of Mn and Fe atoms. During the steps of oxygen release and storage, this network, deriving from the rocksalt framework, seems to preserve the Fe and Mn organization at the local scale.

INTRODUCTION. The effects of redox treatments on the chemical/structural behavior of Transition Metal (TM)-based oxides have attracted much attention principally because of their use as OSC (Oxygen Storage Capacity) promoters in heterogeneous catalysis or as positive electrodes in fuel cells and Li/Na batteries. In both cases, the application requires the stabilization of TM at high oxidation states. The reversible intercalation/deintercalation of alkaline and alkaline earth into oxide frameworks in order to tune the TM oxidation states during the cycling of batteries as well as the reversible variation of the oxygen stoichiometry into solid oxide fuel cells are key features. The oxygen deficiency in rare-earth based oxides with fluorite type networks or in transition metal based oxides with perovskite structure is of particular interest because of the stabilization of various oxidation states in different environments that can considerably influence their oxidation-reduction catalytic properties.[1, 2, 3, 4] In order to achieve high efficiency for OSC promoters or catalytic converters, tetravalent TM are generally partially stabilized in oxides during oxidation. During the reduction process, divalent TM can be also identified. In these conditions the largest variations of TM oxidation states favor the highest rates of exchanged oxygen with an efficient redox power. Among M transition metals, Ni, Co, Fe and Mn in +2, +3 and +4 valence states can be stabilized in oxygen non-stoichiometric perovskite RMO_{3-x} (R: rare-earth or alkaline-earth) with corner-sharing MO_n (n integer, $4 \leq n \leq 6$) polyhedra or in alkaline-A non-stoichiometry layered compounds A_xMO_2 with edge-sharing MO_6 octahedra to form rocksalt-related sheets.[5, 6, 7, 8, 9, 10, 11, 12] Because of their lower toxicity, active Fe and Mn are of considerable importance but it is difficult to stabilize Fe^{2+} ($3d^6$) and Mn^{2+} ($3d^5$) in these frameworks due mainly to the large ionic size of these ions when stabilized in octahedral coordination. Then, in order to identify such reduced states in perovskite structures, it is often necessary to lower the coordination number of these transition metals induced by oxygen non-stoichiometry. For instance, in $La_{0.5}Sr_{0.5}MnO_{2.5}$[13] or $SrFe_{1-x}Mn_xO_2$ ($0 \leq x \leq 0.2$)[14] phases, Mn^{2+} can be stabilized in tetrahedral or square planar environments respectively.

Very few Fe and Mn-based complex oxides and related structures can be stabilized either with +4 oxidation state under oxidizing atmosphere or +2 valence state under reducing conditions without exhibiting phase separation. For instance, the $SrFeO_3$ (Fe^{4+}-$3d^4$- stabilized in octahedral site)[15] and $SrFeO_2$ (Fe^{2+} -$3d^6$- stabilized in square planar coordination)[16] phases with perovskite related structure can be quoted. Furthermore it is worth noting that the reduction process of $CaMnO_{3-x}$ perovskite-type oxide into $CaMnO_2$ rock-salt type network (or the reversible transformation of corner-sharing 3D network of Mn^{4+} octahedral sites into edge-sharing 3D framework of Ca^{2+}/Mn^{2+} octahedral environments) occurs despite the difference of ionic radii.[17] .Furthermore, ordering of Ca^{2+} and Mn^{2+} ions at the nanoscale into distorted rhombohedral cell deriving from rocksalt network, has been shown. By exploring the $CaO\text{-}MnO_{2-x}$ ternary phase diagram,[18] the Ca-rich

domain reveals the existence of corner-sharing $Mn^{4+}O_6$ octahedra associated with perovskite or Ruddelsden-Popper phases whereas the Mn-rich zone is related to edge-sharing and corner-sharing MnO_6 (Mn^{4+}/Mn^{3+}) octahedra describing a 3D tunnel network in the case of the $CaMn_3O_6$ composition. For this latter example, two rutile double-chains with edge-sharing MnO_6 octahedra, related to the rocksalt-type network, are connected one to each other by corner-sharing octahedra[19], thus forming 1D channels where Ca^{2+} ions are located. Special attention has been paid on the reduction-oxidation phenomena in this 3D tunnel network where the building blocks are strongly related to the rocksalt-type network. This structure derives from the $CaFe_2O_4$-type network (SG : Pnma) with two Fe^{3+} atomic positions corresponding to the two rutile double chains but also with a large content of Ca^{2+} vacancies equal to 0.33.[20, 21] The $CaMn_3O_6$ chemical formulae can also be written as '$Ca_{0.66}Mn_2O_4$' which fully describes the $CaFe_2O_4$-type structure. It is worth mentioning the occurrence of Ca^{2+} defects whose rate tends to δ~0.25 in the $Ca_{1-\delta}Fe_{2-x'}Mn_{x'}O_4$ solid solution for $x' > 1$[22]. Moreover, the Ca^{2+} vacancies concentration in this series increases regularly with the Mn^{4+} content[22]. The two atomic positions for transition metals are associated with a highly elongated octahedral site containing a large amount of Jahn-Teller Mn^{3+} ($3d^4$) and a more isotropic site which has a preference for Mn^{4+}($3d^3$) but also Fe^{3+}($3d^5$). This was investigated by Mössbauer spectroscopy.[22] Actually, Fe^{3+} ions occupy both atomic positions and the Fe^{3+} occupancy changes in favor of the more isotropic site as the Mn content decreases.[22] In this series, the Mn valence states as well the Fe^{3+} site occupancy will be strongly affected by the concentration of Ca^{2+} vacancies [22]. These authors use $CaCl_2$ as flux in an open system at T=850°C and the Ca vacancies concentration changes in this solid solution. In our work we focused on the stabilization of the highest level of Ca^{2+} deficiency in this series leading to the highest rate of Mn^{4+}. By fixing the Ca vacancies rate, the symmetry of the unit cell as well the site distortion will be accurately analyzed in this series as far as the Mn-rich domain is concerned.

In our strategy, an oxidative synthesis route (self-combustion) allowing an excellent cationic homogeneity has been used in order to achieve frameworks without oxygen deficiency promoting a high content of Mn^{4+} directly related to a large rate of Ca^{2+} vacancies to ensure electroneutrality.

The aim of this work was first to stabilize a high content of oxidized species, such as Mn^{4+}, and consequently the largest content of Ca^{2+} defects into this 3D tunnel framework. The Fe^{3+} rate of substitution for Mn has been progressively increased in order to keep a high content of Mn^{4+} with the same Ca^{2+} concentration. Then, after identifying the minimum Ca concentration associated with the maximum number of Ca defects within this series with a high rate of Mn^{4+}, we report on structural features of the new $Ca_{0.7}Mn_{2-x}Fe_xO_4$ solid solution ($0 < x \leq 0.6$) refined by Rietveld analysis of powder XRD data. The Fe oxidation state, sites distribution and distortion were investigated by Mössbauer spectroscopy. Finally, the reduction-oxidation process has been monitored by thermogravimetric analysis under reducing and oxidizing atmosphere. Special attention has been paid to the Fe oxidation states as well as the Fe site distribution and distortion observed during the redox cycling.

EXPERIMENTAL SECTION. $Ca_{0.66}Mn_2O_4$ and the complex $Ca_{0.7}Mn_{2-x}Fe_xO_4$ oxides ($0 < x \leq 0.60$) have been prepared by aqueous self-combustion synthesis method (GNP : Glycine Nitrate Process) using glycine,[23, 24, 25] (1 M) Ca^{2+} and (1 M) Mn^{2+} nitrates solutions and $Fe(NO_3)_3\,9H_2O$ powder. Stoichiometric amounts of Ca, Mn and Fe nitrates have been mixed under stirring with a total volume of water around 25 mL for 2 grams of expected oxide. The powdered glycine has been added with a glycine/metal molar ratio equal to 2 in order to ensure an optimum cation chelation. The solution was then heated at 100°C on a hot plate in stainless steel beaker to evaporate water excess and induce the polycondensation of glycine. Self-combustion of the as-obtained viscous solution was carried out on a hot plate at T=220°C in 4 L stainless-steel beaker covered with an openwork lid to prevent the departure of ashes. The as-obtained poorly crystallized ashes were afterwards fired under air at T=850°C for 12h.

Powder X-Ray diffraction patterns have been collected on a Phillips X'Pert MPD X-ray diffractometer operating in Bragg-Brentano geometry with Cu $K\alpha_1/K\alpha_2$ radiations ($10° < 2\theta < 80°$ range, step 0.017° and counting time 500 s) or Cu $K\alpha_1$ radiation (λ=1.5406 Å, $10° < 2\theta < 80°$ range, step 0.008° and counting time 2000 s). The structural parameters (unit cell parameters, atomic positions and occupancies and Debye-Waller factors) have been refined using the Rietveld method and Fullprof® programs with conventional reliability factors. Three different Debye-Waller factors have been determined for Ca, Mn/Fe and O atomic positions, respectively. Due to very close atomic numbers, no difference has been made between Mn and Fe atoms.

Mössbauer measurements were performed at room temperature using a constant acceleration Halder-type spectrometer with a room temperature ^{57}Co source (embedded in a Rh matrix) in transmission geometry. The velocity was calibrated using pure α-Fe as standard material. The analysis of ^{57}Fe Mössbauer spectra was performed using homemade programs and the WinNormos® software.

The thermogravimetric analysis (TGA) was carried out on a SETARAM Setsys Evolution apparatus under reductive (Ar/5% H_2 flux, 50 mL/min) or oxidative (air flux, 50 mL/min) conditions, with a heating rate of 10°C/min or 2°C/min and up to T=550°C or T=700°C, depending on the redox or thermodynamic processes that had to be enlightened.

Samples for transmission electron microscopy (TEM) were prepared by suspending the powder in alcohol by ultrasonication and depositing a drop of the suspension on a copper grid covered with a carbon film. The grid was finally air-dried for 15 min. TEM, high resolution TEM (HRTEM) and scanning TEM coupled with energy dispersive X-Ray spectroscopy (STEM-EDX) observations were performed using a JEOL 2200 FS equipped with a field emission gun, operating at 200 kV and with a point resolution of 0.23 nm. High-resolution transmission electron microscopy micrographs and videos were acquired with a Gatan Ultrascan CCD 2k - 2k and digital diffractograms were calculated using the Gatan Digital Micrograph program. Moreover, in order to be representative and statistically meaningful, many images from several regions of various samples were recorded and the most characteristic results are presented here.

RESULTS AND DISCUSSION.

1. Structural analysis by powder X-ray diffraction

In order to determine the highest Ca vacancy amount that can be stabilized to promote the manganese valency increase, the comparison between the XRD diagrams of $Ca_{0.66}Mn_{1.40}Fe_{0.60}O_4$

(*i.e.* $CaMn_{2.1}Fe_{0.9}O_6$) and $Ca_{0.70}Mn_{1.40}Fe_{0.60}O_4$ compositions is made. It shows the presence of $(Mn,Fe)_2O_3$ bixbyite-type oxide (SG: Ia-3, a=9.431(4) Å) as impurity (Figure 1) in the case of the targeted nominal $Ca_{0.66}Mn_{1.40}Fe_{0.60}O_4$ composition. The lowest Ca rate stabilized within this solid solution is then equal to 0.7 and is associated with the $Ca_{0.7}Mn_{2-x}Fe_xO_4$ chemical formula for the solid solution. Previous studies on $Ca_{1-\delta}Fe_{2-x'}Mn_{x'}O_4$ ($0.44 \leq x' \leq 2.00$) phases have evidenced that the highest Ca vacancies rate was equal to δ=0.25.[22]

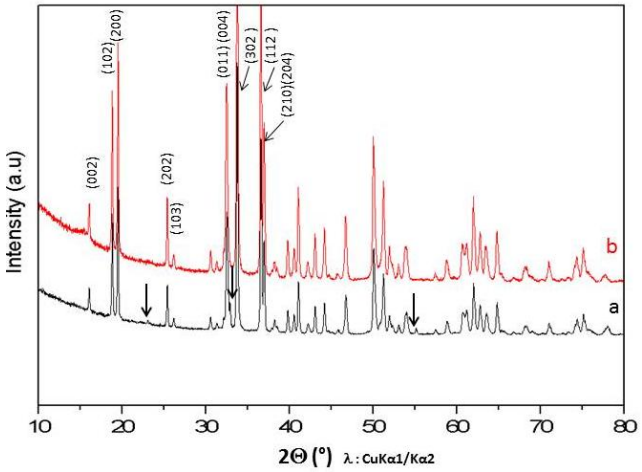

Figure 1: X-ray powder diffraction patterns of a) $Ca_{0.66}Mn_{1,40}Fe_{0.60}O_4$ and b) $Ca_{0,7}Mn_{1,4}Fe_{0,6}O_4$ compounds. For the $Ca_{0.66}Mn_{1.40}Fe_{0.60}O_4$ composition, a small amount of a secondary $(Mn,Fe)_2O_3$ bixbyte-type phase (Cubic unit cell, SG: Ia-3, a=9.431(4) Å) is observed (black arrows). Some (hkl) indexations corresponding to Pnma space group ($CaFe_2O_4$-type) are mentioned.

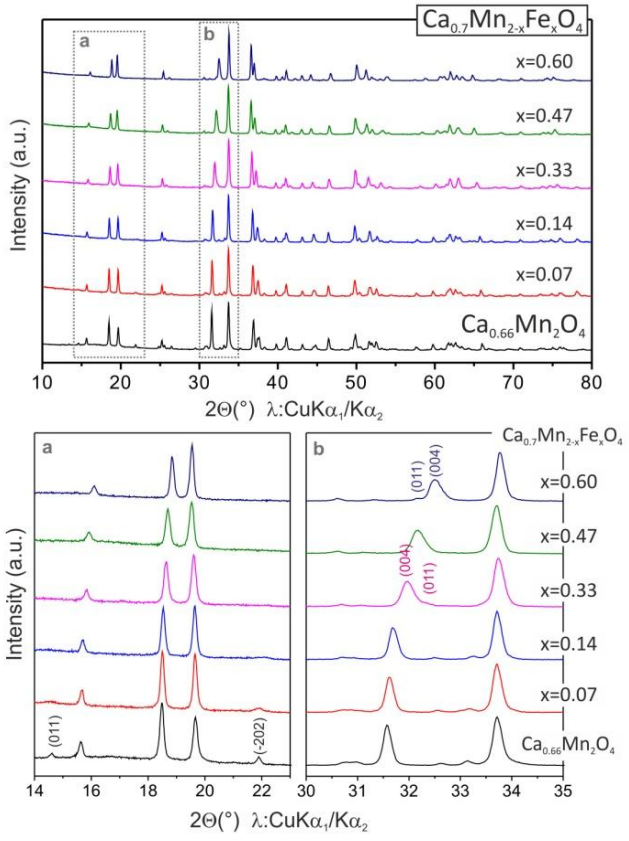

Figure 2: X-ray powder diffraction patterns of $Ca_{0.7}Mn_{2-x}Fe_xO_4$ ($0 < x \leq 0.60$) and $Ca_{0.66}Mn_2O_4$ compounds.

Thus, the GNP route seems to favor a slight increase of the Ca defects amount and consequently, a highest Mn^{4+} content. The powder XRD patterns of $Ca_{0.7}Mn_{2-x}Fe_xO_4$ ($0 < x \leq 0.60$) and $Ca_{0.66}Mn_2O_4$ compounds are presented on Figure 2. For the lowest Fe rates ($x \leq 0.14$), one should notice the occurrence of small intensity diffraction lines corresponding to the monoclinic unit cell (for instance (011) at 2θ=15° and (-202) at 2θ=22°). However, it is worth noting that superstructure diffraction lines observed for the $CaMn_3O_6$ ('$Ca_{0.66}Mn_2O_4$') monoclinic unit cell (SG: P21/a) were not present at low 2θ angles for the Fe-substituted compounds with $x > 0.14$. These ($0.33 \leq x \leq 0.60$) $Ca_{0.7}Mn_{2-x}Fe_xO_4$ compounds crystallize with an orthorhombic unit cell (SG: Pnma) corresponding to the $CaFe_2O_4$-type network (Figure 3).

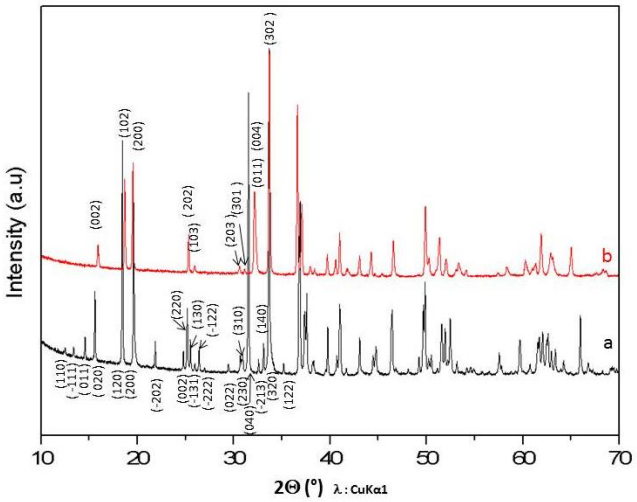

Figure 3: X-ray powder diffraction patterns of a) $CaMn_3O_6 = Ca_{0.66}Mn_2O_4$ (monoclinic unit cell, SG: $P2_1/a$) and b) $Ca_{0.70}Mn_{1.53}Fe_{0.47}O_4$ (orthorhombic unit cell, SG: Pnma) compounds. (hkl) indexations at low 2Θ values are mentioned.

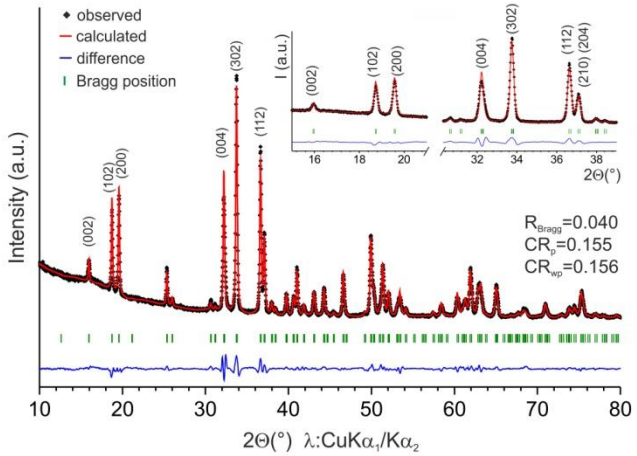

Figure 4: Rietveld analysis of X-ray powder diffraction pattern of $Ca_{0,70}Mn_{1,53}Fe_{0,47}O_4$ compound.

The structural parameters of these iron-rich compounds were refined from powder XRD data (Figures 4, S1 and S2) using the Rietveld method. The results are reported in Tables 1 and 2. Ca^{2+} ions are surrounded by eight oxygen atoms

corresponding to a distorted prism. Moreover, the disorder arising from the occurrence of cationic vacancies could explain the high Debye-Waller factors observed for the Ca^{2+} atomic positions.

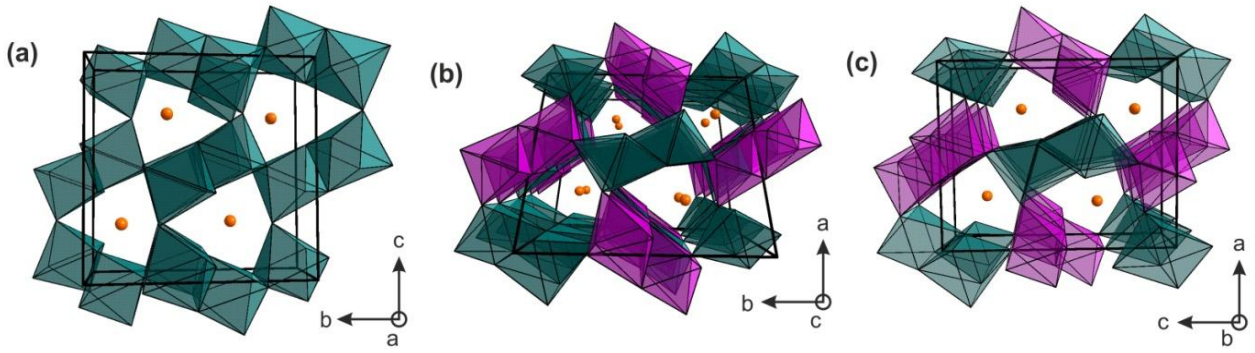

Figure 5: Schematic representation of the structure of a) $CaMn_2O_4$ (orthorhombic unit cell, SG: Pbcm, 1 Mn site), b) $CaMn_3O_6 = Ca_{2/3}Mn_2O_4$ (monoclinic unit cell, SG: P21/a, 6 Mn sites: 2 Mn^{4+} in violet and 4 Mn^{3+} in green) and c) $Ca_{0.70}Mn_{2-x}Fe_xO_4$ (x=0.33, 0.47, 0.60) (orthorhombic unit cell, SG: Pnma, 2Mn(Fe) sites: 1 Mn^{4+}-rich in violet and 1 Mn^{3+} -rich in green) compounds.

Table 1: Atomic positions and unit cell parameters of $Ca_{0.70}Mn_{2-x}Fe_xO_4$ oxides ($0.33 \leq x \leq 0.60$) determined by Rietveld refinement from powder X-Ray diffraction data (λCu Kα_1/Kα_2). The reliability factors CRp, CRpw and RBragg are quoted.

Atomic coordinates – S.G: *P n m a*						
Atom	Wyck.	x(Fe)	x	y	z	B(Å^2)
Ca	4c	0.33	0.2468(5)	¼	0.3331(3)	2.7(1)
		0.47	0.2454(6)	¼	0.3349(4)	2.6(1)
		0.60	0.2437(5)	¼	0.3362(3)	3.1(1)
M1	4c	0.33	0.0678(2)	¼	0.1121(1)	0.8(1)
		0.47	0.0663(3)	¼	0.5997(2)	0.5(1)
		0.60	0.0650(2)	¼	0.1125(1)	1.0(1)
M2	4c	0.33	0.0842(2)	¼	0.5974(1)	0.8(1)
		0.47	0.0849(3)	¼	0.5997(2)	0.5(1)
		0.60	0.0852(2)	¼	0.6001(1)	1.0(1)
O1	4c	0.33	0.2952(7)	¼	0.6588(6)	0.5(1)
		0.47	0.3010(8)	¼	0.6581(7)	0.3(1)
		0.60	0.2984(7)	¼	0.6602(6)	0.5(1)
O2	4c	0.33	0.3793(6)	¼	0.9758(6)	0.5(1)
		0.47	0.3788(7)	¼	0.9757(7)	0.3(1)
		0.60	0.3809(7)	¼	0.9772(6)	0.5(1)
O3	4c	0.33	0.4711(7)	¼	0.2029(5)	0.5(1)
		0.47	0.4681(8)	¼	0.2074(6)	0.3(1)
		0.60	0.4678(7)	¼	0.2072(5)	0.5(1)
O4	4c	0.33	0.0804(9)	¼	0.9166(5)	0.5(1)
		0.47	0.0829(9)	¼	0.9181(6)	0.3(1)
		0.60	0.0778(7)	¼	0.9211(5)	0.5(1)

Unit cell parameters				
x(Fe)	a (Å)	b (Å)	c (Å)	V (Å^3)
0.33	9.0445(1)	2.8542(1)	11.1850(4)	288.74(2)
0.47	9.0708(5)	2.8664(1)	11.1102(6)	288.88(3)
0.60	9.0877(7)	2.8765(2)	11.0167(8)	287.99(4)

Rietveld reliability factors			
x(Fe)	CRp (%)	CRwp (%)	RBragg (%)

0.33	13.6	14.0	4.4
0.47	15.5	15.6	4.0
0.60	13.9	15.1	3.8

Table 2: Bond distances calculated from Rietveld refinement of $Ca_{0.70}Mn_{2-x}Fe_xO_4$ ($0.33 \leq x \leq 0.60$) structural parameters (see Table 1). The average <M-O> and <Ca-O> bonds distances as well as the average of the difference between main distance and average distance are mentioned.

Distances (Å)			
x(Fe)	0.33	0.47	0.60
M1-O1	1.960(4) x 2	1.944(3) x 2	1.971(4) x 2
M1-O3	2.246(6)	2.206(7)	2.173(6)
M1-O4	1.984(5) x 2	1.997(5) x 2	1.972(4) x 2
	2.190(5)	2.147(7)	2.112(5)
<M1-O>	2.054	2.039	2.028
|M1-O - <M1-O>|/6	0.109	0.092	0.076
M2-O1	2.027(6)	2.064(8)	2.047(6)
M2-O2	1.999(4) x 2	2.0115(5) x 2	1.999(4) x 2
	2.026(5)	2.048(1)	2.043(6)
M2-O3	1.917(4) x 2	1.928(4) x 2	1.921(3) x 2
<M2-O>	1.981	1.999	1.989
|M2-O - <M2-O>|/6	0.042	0.048	0.045
Ca-O1	2.445(6) x 2	2.467(7) x 2	2.444(6) x 2
Ca-O2	2.425(5) x 2	2.402(7) x 2	2.400(6) x 2
Ca-O3	2.497(7)	2.467(8)	2.483(7)
	2.525(7)	2.558(9)	2.552(7)
Ca-O4	2.313(6) x 2	2.309(7) x 2	2.361(5) x 2
<Ca-O>	2.424	2.423	2.431
|Ca-O - <Ca-O>|/8	0.055	0.067	0.050

Concerning the transition metal ions, $Mn^{3+/4+}$ and Fe^{3+}, two different octahedral sites can be identified on the basis of bond distances (Table 2). The first site (M1) is highly distorted with four short bond distances (~1.97 Å) and two longer ones (~2.20 Å) whereas the second (M2) is more regular with M-O bond length varying from 1.92 to 2.05 Å. In a first approximation and taking into account the average distortion for each site, the M2 site will be more suitable for Mn^{4+} because it is smaller and isotropic while the largest and distorted M1 site is consistent with the presence of Jahn-Teller Mn^{3+} (see figure 5). While Mn^{3+} is distributed on both sites (the global valency of manganese orders the presence of Mn^{3+} in M2 site also), Mn^{4+} is expected to be localized only in the most symmetric one. The M1 octahedron becomes more regular as the Fe^{3+} concentration increases. Indeed, the M1-O bond-lengths range from 1.96 to 2.25 Å for x=0.33 and from 1.97 to 2.17 Å for x=0.60 while the deviation $|$M1-O - <M1-O>/6$|$ decreases as x increases. Thus, the replacement of the Mn^{3+} Jahn--Teller ion by the isotropic Fe^{3+} ion in the M1 site contributes to decrease the octahedron distortion. Furthermore, the less distorted site (M2) does not seem to be affected by the iron content (within the investigated range). However, due to the fact that Mn^{3+} and Fe^{3+} in isotropic environment adopt the same size (0.645 Å), the presence of Fe^{3+} in the M2 site cannot be excluded.

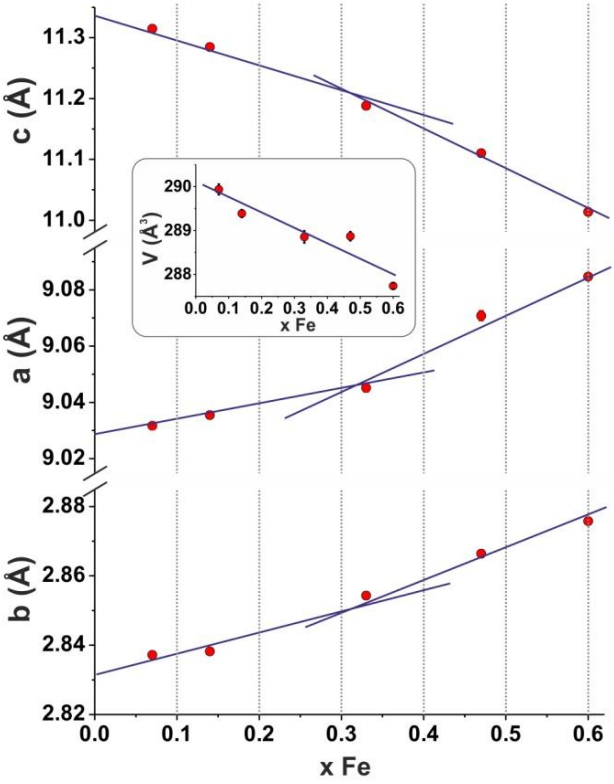

Figure 6: Evolution with iron content (x Fe) of unit cell parameters of $Ca_{0.70}Mn_{2-x}Fe_xO_4$ ($0.07 \leq x \leq 0.60$) compounds (orthorhombic unit cell, SG:Pnma). Inset: Evolution with x Fe of the unit cell volume. Solid lines are a guide to the eye.

Considering the following relationship between the monoclinic (SG: $P2_1/a$) and the orthorhombic (SG: Pnma) unit cells:

$(a_m, b_m, c_m) = (a_o, b_o, c_o)\begin{bmatrix}1 & 0 & 0\\ 2 & 0 & -3\\ 0 & 1 & 0\end{bmatrix}$, the monoclinic and the orthorhombic unit cells parameters have been refined for the whole solid solution and their variations described in an orthorhombic unit cell are represented on Figure 6. The cell parameters follow a monotonous evolution with the Fe content with a change of slope around x=0.33 when the symmetry of the unit cell becomes orthorhombic, which confirms the Fe substitution for Mn. The c parameter undergoes the most pronounced variation (decrease) versus x while a and b slightly increase as the iron content increases. The apical axis of Mn^{3+}-rich octahedra (site M1) lies along the c axis while their square plane mainly belongs to the (a, b) plane. In this

way, the substitution of Mn^{3+} for Fe^{3+} implies a decreasing of the Jahn-Teller distortion, *i.e.* a contraction of the apical axis and an expansion of the square plane which is fully consistent to the experimental observations. Moreover, the Fe^{3+} (with $t_{2g}^3e_g^2$ electronic configuration) partial substitution for Mn^{3+} ($t_{2g}^3e_g^1$) ions contributes to decrease the Mn/Fe-Mn/Fe direct interactions *via* the t_{2g} orbitals by enlarging the distance between two edge-sharing octahedra. It leads also to an increase of b which is related to the Mn/Fe-Mn/Fe distance between two edge-sharing octahedra into the rutile double chains (Figure 5). Because the M2 site is mainly occupied by Mn^{4+} ions which favor an isotropic environment, if the substitution of Mn^{3+} for Fe^{3+} (equivalent in size) is efficient in this site, it does probably not impact significantly the cell parameters.

2. Fe local environment investigation by ^{57}Fe Mössbauer spectroscopy.

The Mössbauer spectra of $Ca_{0.7}Mn_{2-x}Fe_xO_4$ ($0.07 \leq x \leq 0.60$) can be interpreted as the sum of two signals (Figure 7), whose parameters (isomer shift and quadrupole splitting) are characteristic of trivalent iron ions in octahedral environment (Table 3). Each signal, denoted Fe(1) or Fe(2), may actually be analyzed as the sum of quadrupole doublets with lorentzian shape (linewidth: 0.28 mm/s), same isomer shift but different quadrupole splitting values (*i.e* with a distribution of quadrupole splitting values). Considering that Fe^{3+} is in a high-spin state and that the $^6A_{1g}$ (^6S) ground state has a spherically symmetric distribution of electronic charge, the quadrupole splitting arises mainly from the lattice contribution to the electric field gradient (EFG) through the crystal field produced by ligands at the ^{57}Fe nucleus. Then, a distribution of quadrupole splitting may reflect slight variations of the EFG (at iron sites) due to some local disorder or heterogeneity in site distortion, for example. Regarding the isomer shifts, the shapes and mean values of the quadrupole splitting distribution (Table 3 and figure 7), Fe(1) and Fe(2) signals can be associated with Fe^{3+} ions located in two distinct octahedral sites with different degrees of distortion.

For low Fe contents associated with the monoclinic symmetry of the unit cell, Fe^{3+} evidences a slight preference for the less distorted site with the lower quadrupole splitting value (0.6 – 0.7 mm/s) and a monomodal distribution (figure 7). When the symmetry becomes orthorhombic with two Mn/Fe atomic positions, the relative proportion of the two Fe^{3+} Mössbauer signals tends to 50:50. Moreover, as the Fe^{3+} concentration increases, the distribution of the Fe(1) quadrupole splitting clearly becomes multimodal and its mean value decreases whereas the quadrupole splitting of the second signal Fe(2), associated with the less distorted crystallographic site, remains almost constant. This result is in very good agreement with the XRD analysis previously described. For low Fe doping rate, Fe^{3+} ions prefer the most regular site occupied mainly by Mn^{4+} (t_{2g}^3) because of its electronic configuration $t_{2g}^3e_g^2$. For higher Fe content, Fe^{3+} ions occupy both Mn^{3+} and Mn^{4+}-rich sites in an orthorhombic unit cell.

Table 3: ^{57}Fe Mössbauer hyperfine parameters (δ: isomer shift, <Δ>: mean value of quadrupole splitting distribution, lorentzian linewidth: Γ=0.28 mm/s, reference: α-Fe), calculated from Mössbauer spectra of $Ca_{0.70}Mn_{2-x}Fe_xO_4$ ($0.07 \leq x \leq 0.60$) compounds (Figure 7). Chemical formula for both Mn/Fe sites have been deduced from the proportion of Fe^{3+} in more distorted (Mn^{3+}, M1) and less distorted ($Mn^{3+/4+}$, M2) sites.

x(Fe)	Fe(1) (M1)			Fe(2) (M2)			Chemical formula
	δ (mm/s)	<Δ> (mm/s)	Area (%)	δ (mm/s)	<Δ> (mm/s)	Area (%)	$[Mn/Fe]^{M1}\,[Mn/Fe]^{M2}$
0.07	0.353	1.50	33	0.348	0.73	67	$[Mn_{0.98}^{3+}Fe_{0.02}^{3+}]^{M1}\,[Mn_{0.60}^{4+}Mn_{0.35}^{3+}Fe_{0.05}^{3+}]^{M2}$
0.14	0.359	1.37	46	0.347	0.64	54	$[Mn_{0.94}^{3+}Fe_{0.06}^{3+}]^{M1}\,[Mn_{0.60}^{4+}Mn_{0.32}^{3+}Fe_{0.08}^{3+}]^{M2}$
0.33	0.357	1.29	47	0.354	0.66	53	$[Mn_{0.84}^{3+}Fe_{0.16}^{3+}]^{M1}\,[Mn_{0.60}^{4+}Mn_{0.23}^{3+}Fe_{0.17}^{3+}]^{M2}$
0.47	0.357	1.19	49	0.354	0.65	51	$[Mn_{0.77}^{3+}Fe_{0.23}^{3+}]^{M1}\,[Mn_{0.60}^{4+}Mn_{0.16}^{3+}Fe_{0.24}^{3+}]^{M2}$
0.60	0.361	1.07	52	0.359	0.61	48	$[Mn_{0.68}^{3+}Fe_{0.32}^{3+}]^{M1}\,[Mn_{0.60}^{4+}Mn_{0.12}^{3+}Fe_{0.28}^{3+}]^{M2}$

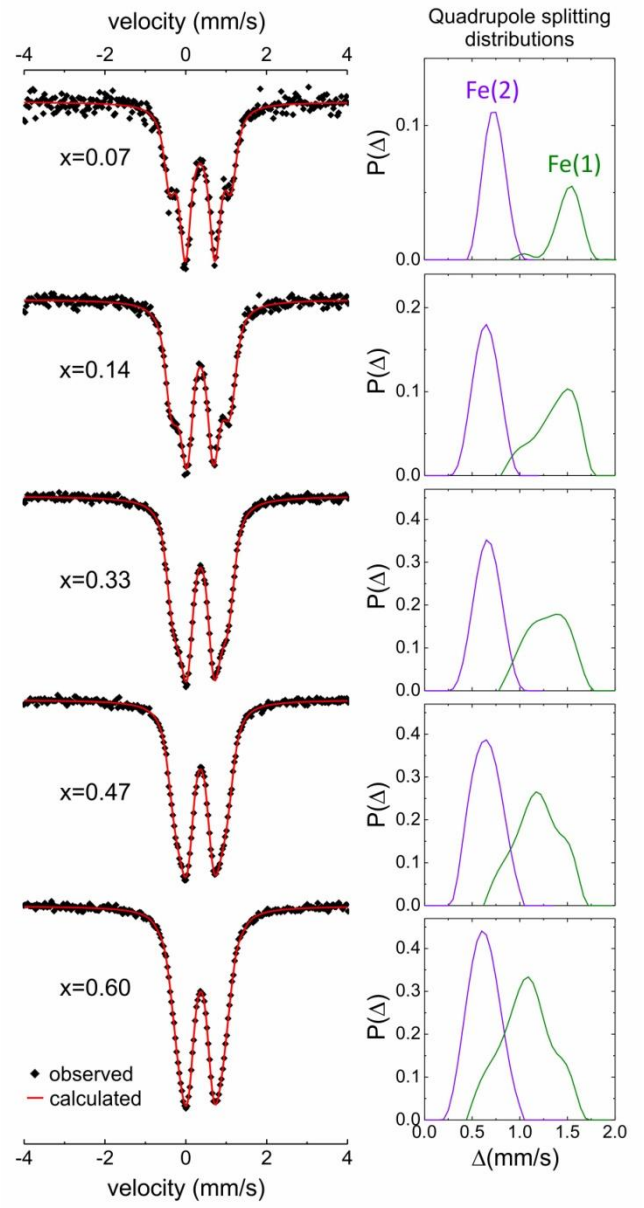

Figure 7: ^{57}Fe Mössbauer spectra of $Ca_{0.70}Mn_{2-x}Fe_xO_4$ ($0.07 \leq x \leq 0.60$) compounds (at room temperature).

On the basis of Mössbauer investigation and especially the refinement of the relative proportion of Fe^{3+} signals, the Mn valence states distribution have been estimated considering, as a first approximation, that all Mn^{4+} ions occupy the most regular octahedra associated with the lower quadrupole splitting values (Table 3). Then, the Mn^{3+} content occupying mainly the most distorted octahedral site can be deduced. It is worth mentioning that the variation of the highest quadrupole splitting (Fe(1) signal on Figure 7) *versus* the as-determined Mn^{3+} rate is monotonous (Figure S3), showing the correlation between the Fe site distortion and the Mn valence states distribution. Thus, the change of symmetry from monoclinic to orthorhombic appears to have a significant impact on the Fe^{3+} site distribution.

3. Thermal stability and redox properties of new $Ca_{0.70}Mn_{2-x}Fe_xO_4$ ($0 < x \leq 0.60$)

The thermal stabilities of one Fe-doped manganite ($Ca_{0.70}Mn_{1.53}Fe_{0.47}O_4$) and pure $Ca_{0.66}Mn_2O_4$ oxide have been investigated by XRD after annealing of the compounds at different temperatures under air (Figures S4 and S5). A significant improvement of the thermal stability was observed as the substituted composition is still stable after annealing at 1000°C while $Ca_{0.66}Mn_2O_4$ decomposes when treated at 850°C. Thus, the distribution of Fe^{3+} in both M1 and M2 sites (Tables 1 and 2) leads to stabilization of the material as the substituting ion acts as anchor point in the network.

Typical thermogravimetric analyses (and first derivative curves dTG) corresponding to $Ca_{0.70}Mn_{1.53}Fe_{0.47}O_4$ and $Ca_{0.66}Mn_2O_4$ compositions are presented on Figure 8. The reduction process of the Fe-substituted oxide is clearly shifted towards higher temperatures (Table 4). This variation is in good agreement with the increase of the Mn-O chemical bonding covalence related to the presence of Fe^{3+} ions (with a higher electronegativity than Mn) which induces a contraction of the unit cell (volume decrease on Figure 6). For $Ca_{0.7}Mn_{1.53}Fe_{0.47}O_4$, three major steps can be identified in the reduction process. The first step occurs between T=320°C and T=450°C, the second one between T=450°C and T=540°C and the last one takes place at T> 550°C.

During the first step, at the inflexion point (T=380°C), the weight loss $\Delta m/m = 2.4$ % ($\Delta O(Mn) = 0.19$, exchanged oxygen atom per manganese) could be related to the reduction of Mn^{4+} ions into Mn^{3+} ions corresponding to the intermediate chemical formula:

$Ca_{0.70}(Mn_{0.79}{}^{3+}Fe_{0.21}{}^{3+})^{M(1)}(Mn_{0.60}{}^{3+}Mn_{0.15}{}^{3+}Fe_{0.25}{}^{3+})^{M(2)}O_{3.7}$

At T=450°C (first-derivative maximum) which corresponds to the end of this first reduction step, the weight loss 4,8 % ($\Delta O/(Mn) = 0,4$) could be associated with the following chemical formula:

$Ca_{0.7}(Mn_{0.79}{}^{3+}Fe_{0.21}{}^{3+})^{M(1)}(Mn_{0.60}{}^{2+}Mn_{0.15}{}^{3+}Fe_{0.25}{}^{3+})^{M(2)}O_{3.4}$

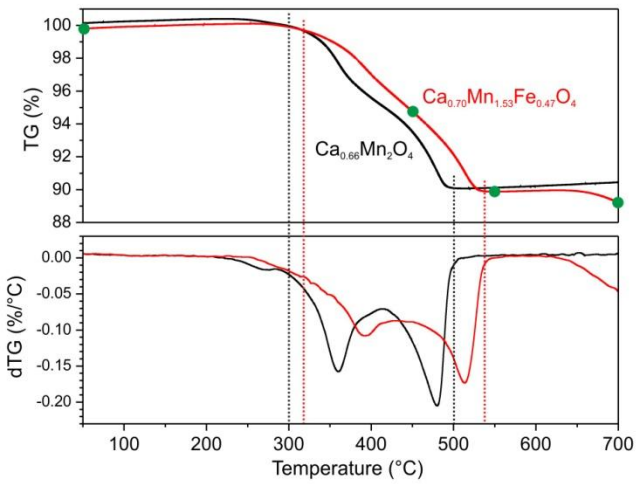

Figure 8: Thermogravimetric analysis (dTG: first derivative curve) of $Ca_{0.70}Mn_{1.53}Fe_{0.47}O_4$ and $Ca_{0.66}Mn_2O_4$ oxides. Experiment was performed from room temperature up to 700°C at heating rate 2°C/min and under Ar/5% H_2 flow. For each compound, the temperature range and the $\Delta m/m$ (Table 4) are determined between the dash lines (black and red). Green dots on TG curve correspond to reduced samples analyzed by Mössbauer spectroscopy (Figures 10 & S6).

This seems consistent with the fact that this first step corresponds to the full reduction of Mn^{4+} ions into Mn^{2+} ions. The reduction of Fe^{3+} and Mn^{3+} ions (initially present in the starting oxidized material) may thus occur at higher temperatures (T > 450°C). This hypothesis was confirmed concerning iron by Mössbauer analysis of the compound obtained after TGA up to 450°C that did not reveal any signatures of Fe^{2+} or Fe^0 (Figure S6). Moreover, the evolution with temperature of the shape and average position of the quadrupole splitting distributions is consistent with a change of iron local environment (site distortion and cationic first-neighbours).

Table 4: Results of thermogravimetric analysis (TGA) performed from room temperature to 700°C at heating rate 2°C/min under Ar/5% H_2 flow for $Ca_{0.66}Mn_2O_4$ and $Ca_{0.7}Mn_{1.53}Fe_{0.47}O_4$ oxides (Figure 8). The ΔO(Mn/Fe) (exchange oxygen atom per manganese and iron) theoretical values have been estimated by considering the total reduction of $Mn^{3+/4+}/Fe^{3+}$ into Mn^{2+}/Fe^{2+}.

		$Ca_{0.66}Mn_2O_4$	$Ca_{0.70}Mn_{1.53}Fe_{0.47}O_4$
Temperature range (°C)		250 – 500	320 – 540
Δm/m (%)	Exp.	10.40	10.30
	Theo.	10.65	10.30
ΔO (Mn/Fe)	Exp.	0.66	0.65
	Theo.	0.67	0.65
Chemical formula after reduction (up to 700 C)		$Ca_{0.25}Mn_{0.75}O$	$Ca_{0.27}Mn_{0.58}Fe_{0.15}O$ + 0.03 Fe^0

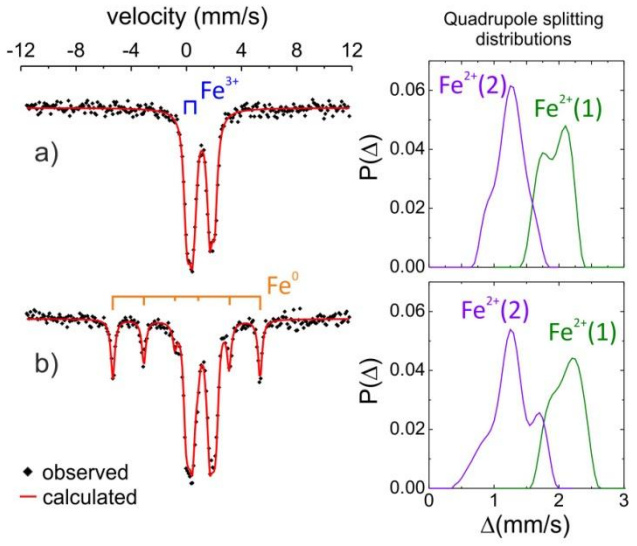

Figure 9: Room temperature ^{57}Fe Mössbauer spectra of $Ca_{0.7}Mn_{1.53}Fe_{0.47}O_4$ compound reduced under Ar / 5 % H_2 from room temperature up to a) 550°C and b) 700°C (TGA experiment performed at heating rate 2°C/min, Figure 8)

Furthermore, the weight loss observed in the temperature range 320°C (beginning of first step) – 540°C (end of second step) (table 4) is compatible with the reduction of both Mn^{4+}/Mn^{3+} and Fe^{3+} species into Mn^{2+} and Fe^{2+}, respectively. The third and last step, observed above 550°C, is related to the reduction of Fe^{2+} ions into metallic iron Fe^0, revealed by ^{57}Fe Mössbauer spectroscopy (Figure 9b) and STEM-EDX analyses (Figure 12-2).

Table 5: ^{57}Fe Mössbauer hyperfine parameters (δ: isomer shift, Γ: linewidth, <Δ>: mean value of quadrupole splitting distribution, ε: quadrupole shift, H: hyperfine field), calculated from Mössbauer spectra of figure 9. The chemical formulas with the occurrence of Fe^0 have been deduced from the respective site proportions. * mean value of quadrupole splitting distribution.

	δ (mm/s)	<Δ> (mm/s)	ε (mm/s)	H (T)	Γ (mm/s)	area (%)
$Ca_{0.7}Mn_{1.53}Fe_{0.47}O_4$ after TGA up to 550°C						
Fe^{2+}(1)	1.068	1.93	-	-	0.30	40
Fe^{2+}(2)	1.051	1.25	-	-	0.30	48
Fe^{3+}(3)	0.273	0.74	-	-	0.30	12
Chemical formula : $Ca_{0.26}Mn_{0.56}[Fe^{3+}]_{0.02}[Fe^{2+}]_{0.15}O$						
$Ca_{0.7}Mn_{1.53}Fe_{0.47}O_4$ after TGA up to 700°C						
Fe^{2+}(1)	1.064	2.11	-	-	0.30	32
Fe^{2+}(2)	1.056	1.27	-	-	0.30	42
Fe^0(0)	0.006	-	- 0.004	33.1	0.34	26
Chemical formula : $Ca_{0.27}Mn_{0.60}[Fe^{2+}]_{0.13}O$ + 0.05Fe^0						

The amount of Fe^0 was estimated, from the analysis of the Mössbauer spectrum, to about 5 at.% (Table 5), what is consistent with the weight loss measured from the TGA curve (corresponding to the formation of about 3 at.% of Fe^0). Moreover, the ^{57}Fe Mössbauer spectrum of the reduced compound (TGA up to 700°C, figure 8) clearly exhibits two other contributions (quadrupole doublets Fe(1) and Fe(2), figure 10b) which can undoubtedly be attributed to Fe^{2+} ions in two distinct octahedral environments (δ≈1.0 mm/s, Δ_1≈1.3 mm/s and Δ_2≈2.0 mm/s). These two last signals were also observed in the Mössbauer spectrum of the Fe-substituted oxide reduced by TGA up to 550°C, *i.e.* prior to the formation of metallic iron (Figure 9a). In addition to Fe^{2+} doublets, a small amount of Fe^{3+} (12 % in relative area, table 5 and Fig. 9a) was also detected, revealing that the reduction of Fe^{3+} ions is incomplete after such a thermal treatment (annealing up to 550°C at heating rate 2°C/min and under Ar/5% H_2). Thus, the reduction of the Fe^{3+} ions located at the more regular octahedral site (M2, associated to a quadrupole splitting value lower than 1 mm/s, see Table 3) may occur after that of Fe^{3+} ions located at the M1 site (more distorted and associated to a quadrupole splitting value higher than 1 mm/s).

The redox cyclability of $Ca_{0.7}Mn_{1.53}Fe_{0.47}O_4$ was tested within the TGA apparatus from room temperature up to 700°C (heating rate: 10°C/min) under Ar / 5% H_2 (reduction steps) or air (oxidation step). The TG curves recorded during each step are reported on figure 10.

X-ray diffraction analysis of the product obtained after reduction at T > 600°C (Figure 11) reveals a major phase

which has crystallized with the rocksalt-type structure and a minor one corresponding to metal iron. Indeed, the weight loss reported on table 6 is consistent with the reduction of Fe^{2+} into metallic Fe°. After re-oxidation, the $CaFe_2O_4$-type network is recovered without any trace of metal Fe° (Figure 11). Moreover, the distribution of Fe^{3+} ions among the two octahedral sites, identified by Mössbauer spectroscopy, is still the same, about 50:50, after re-oxidation (Figure S7).

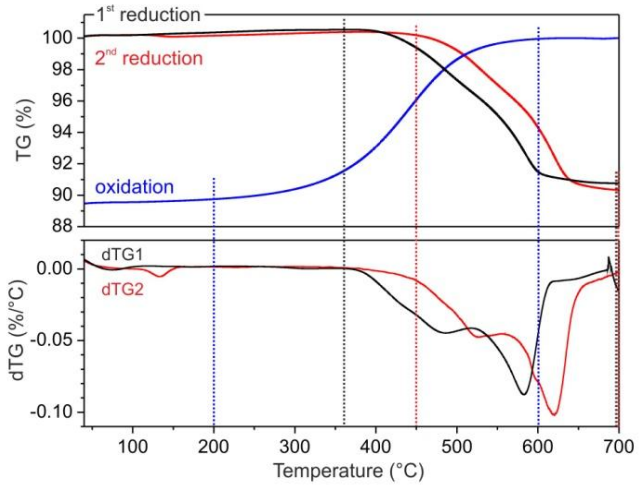

Figure 10: Thermogravimetric analysis (TGA) of $Ca_{0.7}Mn_{1.53}Fe_{0.47}O_4$ oxide. Reduction and oxidation steps are performed from room temperature up to 700°C (heating rate: 10°C/min) under Ar / 5% H_2 flow and under air, respectively. dTG: first derivative curve. For each step, the temperature range and the Δm/m (Table 5) are determined between the dash lines (black, blue and red).

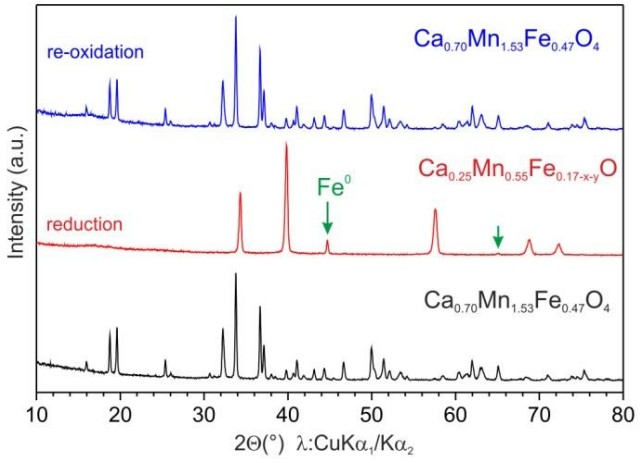

Figure 11: X-ray powder diffraction patterns of $Ca_{0.7}Mn_{1.53}Fe_{0.47}O_4$ oxide (orthorhombic, SG: Pnma) (in black), the mixture of phases (in red), $(Ca_{0.25}Mn_{0.55}Fe_{0.17-x-y})O$ (cubic , SG: Fm-3m) + x Fe^0, obtained after reduction (TGA under Ar/5% H_2, figure 11) and the compound (in blue) recovered after re-oxidation (TGA under air, figure 10) showing the cyclability of this system.

However, the second reduction is significantly shifted towards higher temperatures ($\Delta T \approx +50°C$, Figure 10). Such a phenomenon, occurring after the first redox cycle, could be related to either a change of particle morphology or a reinforcement of the covalency of Mn-O chemical bonds. Some Ca and Fe atoms segregation with a random distribution of Ca^{2+} vacancies, even if the Fe^{3+} site (average) distribution remains the same, should explain such a behavior. Indeed, STEM-EDX analyses have shown some calcium segregation located at grain boundaries (Figure 12-3) and an evolution of the particles morphology after the first reduction.

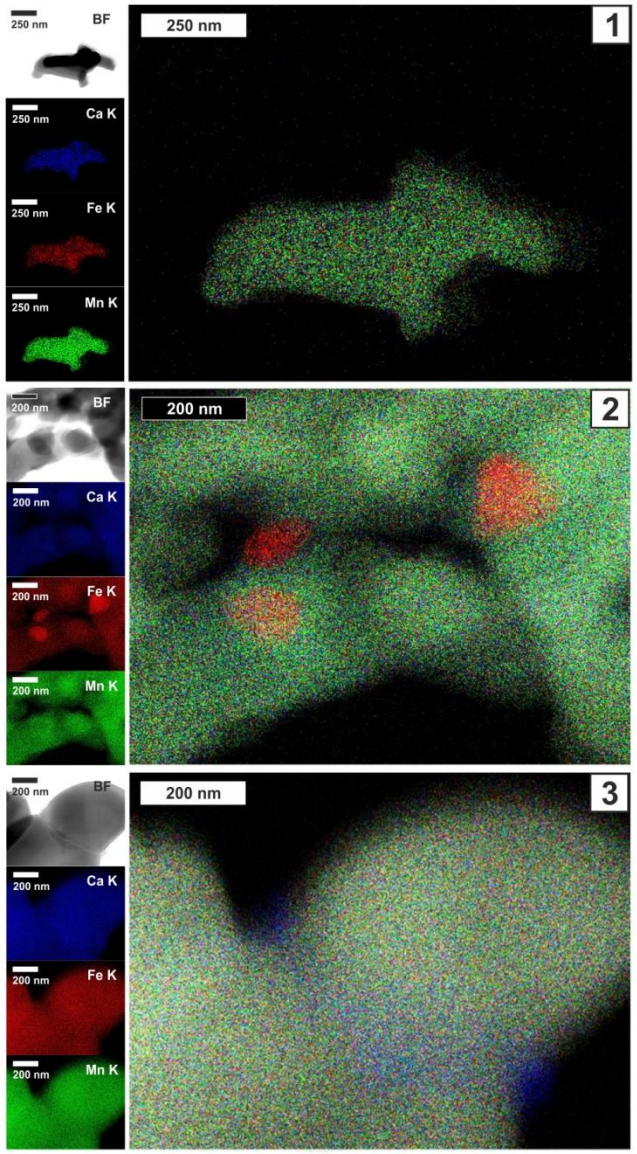

Figure 12: STEM light-field images (BF) and EDX elementary analyses of (1) as-synthesized $Ca_{0,7}Mn_{1,53}Fe_{0,47}O_4$, (2) reduced ($Ca_{0,27}Mn_{0,60}Fe_{0,13}O$ + 0,05Fe^0) and (3) cycled $Ca_{0,7}Mn_{1,53}Fe_{0,47}O_4$ compounds. Right panel: "three colours" images obtained by addition of the three elementary cartographs.

CONCLUSIONS.

Despite the fact that Fe substitution for Mn in the $Ca_{1-\delta}Mn_{2-x}Fe_xO_4$ solid solution with $CaFe_2O_4$-type structure and high concentrations ($\delta \approx 0.25$) of Ca^{2+} vacancies have already been investigated,[22] the lowest concentration of Ca defects associated with the highest Mn average valence state has been reached in this work. The self combustion route (Glycine-Nitrate Process) performed in this work allows oxidative conditions with the highest content of Mn^{4+} (associated with the largest rate of Ca^{2+} vacancies) in this series to be reached. The control of the

proportions of oxidized ions by GNP leads to the design of new solid-solutions. The $Ca_{0.7}Mn_{2-x}Fe_xO_4$ solid solution ($0 < x \leq 0.6$) has been explored for the first time. Two regions were identified: the low Fe^{3+} concentration (up to x = 0.14), which corresponds to a monoclinic symmetry with 6 Mn/Fe atomic positions, and the iron-rich domain ($x \geq 0.33$), which is associated with an orthorhombic symmetry with only two crystallographic sites for transition metals. On the basis of combined XRD and Mössbauer spectroscopy analyses, one highly distorted octahedral environment related to Mn^{3+} and another one more regular site, preferentially occupied by Mn^{4+}, have been identified. By keeping the lowest Ca content in this series, a clear change of symmetry versus Fe content has been revealed associated to a modification of the site distortion due to the distribution of Mn^{3+} as a Jahn-Teller ion in various crystallographic sites. Furthermore, on the basis of Mossbauer spectroscopy analysis, for the low Fe content associated with the monoclinic symmetry, Fe^{3+} evidences a slight preference for the less distorted site and occupies with the same proportion, the two crystallographic sites for the orthorhombic phases.

During the reduction of $Ca_{0.7}Mn_{1.53}Fe_{0.47}O_4$ oxide, two steps have been identified between T=300°C and T=600°C. The first stage between T=300°C and T=450°C is associated with the Mn^{4+} reduction into Mn^{2+} ions on the basis of Mossbauer and TGA analyses. The second reduction level takes place between T=450°C and T=600°C with the reduction of Mn^{3+} and Fe^{3+} into Mn^{2+} and Fe^{2} respectively. The $CaFe_2O_4$-type framework is systematically transformed at T=600°C under $Ar/5\%H_2$ into a rocksalt type structure with a random distribution of Ca^{2+}, Mn^{2+} and Fe^{2+} ions with various ionic radii varying between 1.0 and 0.8 Å corresponding to the general formula (Ca,Mn,Fe)O. The stabilization of Fe^{2+} as well as metallic Fe° in a third step at T>600°C were unexpected after reduction and confirmed by Mossbauer spectroscopy analysis. The re-oxidation under air takes place at T=300°C and the pure $Ca_{0.7}Mn_{1.53}Fe_{0.47}O_4$ oxide is recovered at T>700°C with the same distribution of Fe^{3+} in the two transition metal sites. The occurrence of two different Fe^{2+} sites with various octahedral distortion in the reduced phase, as observed for the oxidized phase with the two Fe^{3+} more or less distorted octahedra, illustrates the thermal history of such materials where topotactic transformations occur by keeping local organization at the nanoscale.

The relationship between the rutile double chains in the $CaFe_2O_4$-type framework and the rocksalt-type network is evident and at the origin of the remarkable redox properties of such materials used as oxygen buffers. The presence of Fe partially substituted for Mn in this series is crucial and contributes to increase the Mn^{4+}/Mn rate and consequently the oxidative power, to enhance the thermal stability and, finally, to stabilize metal Fe^0 in reductive atmosphere leading to promote the reactivity of this composite system. When exposed to fluctuations in the redox conditions of the emission exhaust, the Fe metal particles move back to the octahedral site, substituting for Mn environment into Ca manganite 1D tunnel network. Such behavior has already been observed in a Pd-Perovskite catalyst for automotive emissions control, where Pd ions are substituted in octahedral sites partially occupied by Co and Fe cations in an oxidative atmosphere and decomposes into several oxides as well as Pd metal in reductive conditions [26]. In our case the pure 1D tunnel network for the oxidized catalyst and pure rocksalt-type-phase with Fe metal stabilized in reduced atmosphere has been identified during redox cycling. Pure oxide phases are key features to keep good cycling performances. Calcium manganite with perovskite structure can be used as an oxygen electrode material for reversible oxide fuel cells [27] and calcium manganites with 1D tunnel network/rocksalt solid solution with Fe^0 metal as a reversible redox system should be highly active in this application.

ASSOCIATED CONTENT

Supporting Information.

Figures S1 and S2 showing the Rietveld analysis of X-ray powder diffraction patterns of $Ca_{0.7}Mn_{2-x}Fe_xO_4$ compounds (x=0.33, x=0.60) Figure S3 showing the variation of quadruple splitting of Fe(1) Mössbauer signal versus % Mn^{3+} in the site 1 deduced from Fe^{3+} distribution in sites 1 and 2 (Table 3). Figure S4 showing the X-ray powder diffraction patterns of $Ca_{0.7}Mn_{1.53}Fe_{0.47}O_4$ compound annealed at a) 850°C and b) 1000°C under air for 12 hours. Figure S5 showing the X-ray powder diffraction patterns of $Ca_{0.66}Mn_2O_4$ oxide annealed at a) 850°C (in black) and b) 1000°C (in red) under air for 12 hours. Figure S6 showing the room temperature ^{57}Fe Mössbauer spectra and hyperfine parameters for $Ca_{0.7}Mn_{1.53}Fe_{0.47}O_4$ oxides a) as-synthesized, b) after TGA up to 450°C and c) after TGA up to 550°C (TGA under Ar / 5% H_2 flow with heating rate 2°C/min). Figure S7 showing the room temperature ^{57}Fe Mössbauer spectra and hyperfine parameters for $Ca_{0.7}Mn_{1.53}Fe_{0.47}O_4$ oxides a) as-synthesized and b) after redox cycling (coupled with TGA measurements) under Ar / 5% H_2 then under air flow (heating rate 2°C/min).

AUTHOR INFORMATION

Corresponding Author

* alain.demourgues@icmcb.cnrs.fr

Author Contributions

The manuscript was written through contributions of all authors. / All authors have given approval to the final version of the manuscript.

Funding Sources

The authors thank the SOLVAY company for financial support.

REFERENCES

[1] Funabiki, M.; Yamada, T.; Kayano, K. Auto exhaust catalysts. *Catal. Today* **1991**, 10, 33-43.

[2] Kaspar, J. ; Fornasiero, P. ; Hickey. N, Automotive catalytic converters : current status and some perspectives. .*Catal. Today* **2003**, 77, 419-449.

[3] Yamaguchi, H. ; Yamada, A. ; Uwe. H. Jah,-Teller transition of LiMn2O4 syudied by X-Ray Absorption Spectroscopy. *Phys. Rev. B.* **1998**, 58, 8-11.

[4] Motohashi, T. ; Hirano, Y. ; Masubuchi, Y. ; Oshima, K. ; Setoyama, T. ; Kikkawa, S. Oxygen Storage Capacity of Brownmillerite-type $Ca_2AlMnO_{5+\delta}$ and its application to oxygen enriochment. *Chem.Mater.* **2013**, 25, 372-377.

[5] Ohzuhu, T. ; Ueda, A. Why transition metal oxides are the most attractive materials for batteries. for *Solid State Ionics* **1994**, 69, 201-211.

[6] Goodenough, J.B ; Kim, Y. Challenges for rechargeable Li batteries. *Chem Mater*. **2010**, 22, 587-603.

[7] Brock., S.L. ; Duan, N. ; Tian, R.Z. ; Giraldo, O. ; Zhou, H. ; Suib, S.L. A review of porous manganese oxide materials. *Chem Mater*. **1998**, 10, 2619-2628.

[8] Li, Y. ; Wu, Y. Formation of $Na_{0.44}MnO_2$ nanowires via stress-induced splitting of birnessite nanosheets. *Nano. Res*. **2009**, 2, 54-60.

[9] Drits, V.A. ; Silvester, E. ; Gorshkov, A.I. ; Manceau, A. Structure of synthetic monoclinic Na-rich birnessite and hexagonal birnessite : I-Results from X-ray diffraction and selceted-area electron diffraction. *Am. Mineral*. **1997**, 82, 946-961.

[10] Drits, V.A. ; Lanson, B. ; Gorshkov, A.I. ; Manceau, A. Substructure and superstructure of four-layer Ca-exchanged birnessite. *Am. Mineral* **1998**, 83, 97-118.

[11] Pashchenko, A.V. ; Pashchenko, V.P. ; Revenko, Y.F. ; Prokopenko, V.K. ; Shemyakov, A.A. ; Levchenko, G.G. ; Pismenova, N.E. ; Kitaev, V.V. ; Gufan, Y.M. ; Sil'cheva, A.G. ; Dyakonov, V.P. Structure, Phase Transitions, ^{55}Mn NMR, ^{57}Fe Moss-bauer Studies and Magnetoresistive Properties of $La_{0.6}Sr_{0.3}Mn_{1.1-x}Fe_xo_3$",*J. Magn.Magn. Mater* **2014**, 369, 122-126.

[12] Vashook, V. ; Franke, D. ; Vasylechko, L. ; Zosel, J., Rebello, J. ; Ahlborn, K. ; Fichtner, W. ; Schmidt, M. ; Wen, T.-L. ; Guth, U. Electrical conductivity and oxygen non-stoichiometry of the double B mixed perovskite series $La_{0.6}Ca_{0.4}Mn_{1-y}Me_yO_{3-\delta}$ with Me = Fe,Co, Ni and x= 0-0.6. *Solid State. Ionics* **2008**, 179, 1101-1107.

[13] Cortès-Gil, R. ; Ruiz-Gonzalez, M.L. ; Alonso, J.M. ; Garcia-Hernandez, M. ; Hernando, A. ; Vallet-Regi, M. ; Gonzalez-Calbet, J.M. Magnetoresistance in $La_{0.5}Sr_{0.5}MnO_{2.5}$. *Chem. Eur. J* , **2011**, 17, 2709-2715.

[14] Retuerto, M. ; Jimenez-Villacorta, F. ; Martinez-Lope, M.J. ; Fernandez-Diaz, M.T. ; Alonso, J.A. Stabilization and study of $SrMn_{1-x}Fe_xO_2$ with infinite layer structure. *Inorg. Chem* **2011**, 50, 10929-10936.

[15] Wattiaux, A. ; Fournès, L. ; Demourgues, A. ; Bernaben, N. ; Grenier, J.C. ; Pouchard, M. A novel preparation method of the $SrFeO_3$ cubic perovskite by electrochemical means. *Sol. Stat. Com.* **1991**, 77, 489-493.

[16] Kawakami, T. ; Tsujimoto, Y.; Kageyama, H.; Chen, X.-Q. ; Fu, C.L. ; Tassel, C. ; Kitada, A. ; Suto, S.; Hirama, K. ; Sekiya, Y. ; Makino, Y. ; Okada, T. ; Yagi, T. ; Hayashi, N. ; Yoshimura, K. ; Nasu, S. ; Podloucky, R. ; Takano, M. Spin transition in a four-coordinate iron oxide. *Nature. Chem* **2009**, 1, 371-376.

[17] Varela, A. ; de Dios, S. ; Parras, M. ; Hernando, M. ; Fernández-Díaz, M.T. ; Landa-Cánovas, A.R. ; González-Calbet, J.M. Ordered rock-salt related nanoclusters in $CaMnO_2$. *J.Am.Chem. Soc*. **2009**,131, 8660-8668.

[18] Horowitz, H.S. ; Longo, J.M. Phase relations in the Ca-Mn-O system. *Mater. Res. Bull.* **1978,** 13,1359-1369.

[19] Hadermann, J. ; Abakumov, A.M. ; Gillie, L.J. ; Martin, C. ; Hervieu, M. Coupled cations and charge ordering in the $CaMn_3O_6$ tunnel structure. *Chem. Mater.* **2006**, 18, 5530-5536.

[20] Yamanaka, T. ; Uchida, A. ; Nakamoto, Y. Structural transitions of post-spinel phases $CaMn_2O_4$, $CaFe_2O_4$ and $CaTi_2O_4$ under high pressures up to 80 GPa. *Am. Mineral*. **2008**, 93, 1874-1881.

[21] Tsipis, E. ; Pivak, Y. ; Waerenborgh, J. ; Kolotygin, V. ; Viskup, A. ; Kharton, V. Oxygen ionic conductivty, Mossbauer spectra and thermal expansion of $CaFe_2O_{4-\delta}$. *Solid State Ionics* **2007**, 178, 1428-1436.

[22] Yang, T. ; Croft, M. ; Ignatov, A. ; Nowik, I. ; Cong, R. ; Greenblatt, M. Stabilization of $Ca_{1-\delta}Fe_{2-x}Mn_xO_4$ ($0.44<x<2$) with $CaFe_2O_4$-type structure and Ca^{2+} defects in one-dimensionnal (1D) channels. *Chem.Mater.* **2010**, 22, 5876-5886.

[23] Chick, L. ; Pederson, L. ; Maupin, G. ; Bates, J. ; Thomas, L.E. ; Exarhos, G.J. Glycine-nitrate combustion synthesis of oxide ceramic powders. *Mater. Lett*. **1990**, 10, 6-12.

[24] Deshpande, K. ; Mukasyan, A. ; Varma, A. High throughput evaluation of perovskite-based anode catalysts for direct methanol fuel cells. *J. Power Sources* **2006**, 158, 60-68.

[25] Epherre, R. ; Duguet, E. ; Mornet, S. ; Pollert, E. ; Louguet, S. ; Lecommandoux, S. ; Schatz, C. ; Goglio, G. Manganite perovskite nanoparticles for self-controlled magnetic fluid hyperthermia : about the suitability of an aqueous combustion synthesis route. *J. Mater. Chem*. **2011**, 21, 4393-4401.

[26] Nishihata. Y, Mizuki. J, Akao. T, Tanaka. H, Uenishi. M, Kimura. M, Okamoto. T, Hamada. N. Self regeneration of a Pd-perovskite catalyst for automotive emissions control. *Nature*, **2002**, 418, 164-167 .

[27] Ni. C, Irvine. T.S, Calcium manganite as oxygen electrode materials for reversible solid oxide fuel cell. *Faraday Discuss*, **2015**, 182, 289-305